FOI

A Computational Study of Unsteady Gun Tube Flows

CHRISTER FUREBY, CARL TROENG

FOI-R--3663--SE
ISSN 1650-1942 Mars 2013

Christer Fureby, Carl Troeng

A Computational Study of Unsteady Gun Tube Flows

Titel	En numerisk studie av instationär strömning i eldrör
Title	A Computational Study of Unsteady Gun Tube Flows
Rapportnr/Report no	FOI-R--3663--SE
Månad/Month	Mars
Utgivningsår/Year	2013
Antal sidor/Pages	26 p
ISSN	1650-1942
Kund/Customer	Försvarsmakten
FoT område	Vapen och Skydd
Forskningsområde	Vapen, skydd och säkerhet
Projektnr/Project no	E36501
Godkänd av/Approved by	Lars Höstbeck
Ansvarig avdelning	Informations- och aerosystem

Sammanfattning

Denna rapport sammanfattar en numerisk studie av strömningen i ett eldrör utnyttjande en Large Eddy Simulation (LES) modell tillsammans med en ‘deformation and regeneration’ teknik för hantering av projektilens rörelse. En generisk, och enkel, eldrörskonfiguration utan räffling och flamdämpare, har använts för att demonstrera denna teknik. Förutom att använda ‘deformation and regeneration’ tekniken, har adaptiv nätförfining också användas för att förbättra den rumsliga upplösningen mellan stötvågen och eldröret. En analys av simuleringsresultaten visar att en stötvåg, driven av projektilen, fortplantas genom eldröret precis framför projektilen. När stötvågen lämnar eldröret, expanderar den i alla riktningar och följs av en jetstråle av heta gaser. Deras utströmning genom eldrörets mynning resulterar sedan i att en toridformad virvel bildas vid eldrörets mynning. Efter det förflyttar projektilen sig själv vidare under det att den samverkar med de heta gaserna som strömmar ur eldröret samt den föregående stötvågen.

Nyckelord: eldrör, projektil, innerballistik, storvirvelsimulering

Summary

This report summarize a computational study of unsteady gun tube flows based on a Large Eddy Simulation (LES) model coupled with a deformation and regeneration technique for handling the motion of the projectile. A generic, and rather simple, gun tube configuration, without rifling and muzzle brake, has been used to demonstrate this approach. In addition to using the deformation and regeneration technique, semi-adaptive grid refinement is also used to improve the spatial resolution between the precursor bow shock and the gun tube. From the simulation results some analysis is presented regarding the flow within the gun tube and just outside the muzzle. A precursor shock wave driven by the projectile propagates through the gun tube and ahead of the projectile that acts like a piston. When the precursor shock wave discharges from the open end, the first blast develops, which results in shock-wave diffraction with an associated initiation of a vortex ring and a jet flow. Later, the projectile itself moves out and away from the gun tube and interacts with the diffracting shock system and the jet flow. Meanwhile, the high-pressure high-temperature propellant gas behind the projectile expands out of the shock tube and the second blast develops.

Keywords: gun tube, projectile, interior ballistics, large eddy simulation,

Table of Contents

1 Introduction

A typical gun consists of a gun tube (or barrel) open at the muzzle end and equipped with a breach, i.e. a strengthened firing chamber, at the other end. The cartridge packages a projectile, propellant and a primer within a casing that precisely fits within the firing chamber, and is usually inserted into the breach from the breach end. After loading the breach end is closed and the primer is ignited. Energy is the transferred from the hot igniter gas to the propellant until the propellant ignites and burns, releasing chemical energy. Once the propellant combusts the chamber will pressurize rapidly transmitting a force onto the projectile-base. The projectile is held in position by an engraving band which does not allow the projectile to move before the pressure behind it is high – typically around 60 MPa. The engraving band is designed so that once the pressure rises above this level, a torque is created causing the projectile and engraving band to spin out of position and travel along the gun tube. The movement of the projectile extends the length of the combustion chamber until finally the projectile leaves through the muzzle into the outside atmosphere. Usually, the propellant will be completely burnt before the projectile leaves the barrel. The muzzle end of the gun tube is usually fitted with a muzzle break in order to redirect propellant gases with the effect of countering both recoil of the gun and unwanted rising of the barrel during rapid fire.

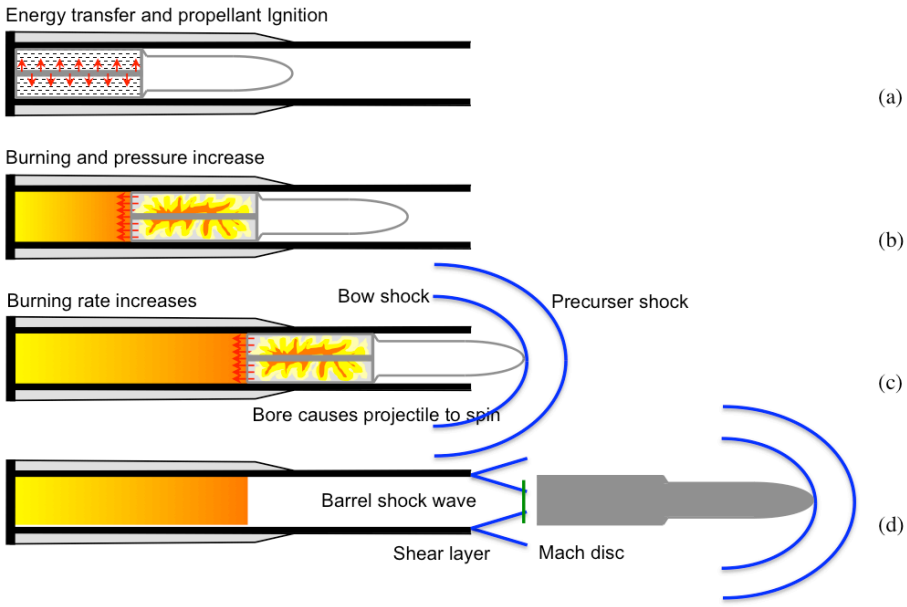

Figure 1. Schematic of a typical ballistic cycle.

Wave dynamic processes occurring in the muzzle blast flow are schematically shown in figure 1 and are briefly described as follows: Assuming that the gun tube has a simple open end to ambient air, in which a projectile moves at a supersonic speed, a precursor shock wave driven by the projectile propagate in the shock tube and ahead of the projectile that acts like a piston. The pressure is higher behind the projectile and lower in front of it due to the friction force between the projectile and the shock tube wall, which maintains a balance between the driving and the drag forces acting on the projectile. When the precursor shock wave discharges from the open end, the first blast develops, which results in shock-wave diffraction with an associated starting vortex ring and a jet flow. Later, the projectile itself moves out of the shock tube and interacts with the diffracting shock system and the jet flow. Meanwhile, the high-pressure gas 'the propellant gas' behind the projectile expands out of the shock tube and the second blast develops. The second blast can

overtake the projectile and the first blast, but these two blasts will be overtaken again later by the projectile. So, this flow field is characterized by two blast waves, two jet flows, and a bow shock wave.

1.1. Review of Previous Work

Early theoretical work on internal ballistics was primarily concerned with calculation of the exit velocity of the projectile, [1]. The force on the projectile is predicted by calculating the pressure history at the projectile-base. Early theory on internal ballistics is well documented in the book by Corber *et al*., [2]. The first models proved to be quite accurate at calculating muzzle velocities and peak pressure but no attempt was made to include flow dynamics in the chamber and the problem was regarded as a 'well-stirred' or 'lumped parameter' system. This means that temporal variation of quantities – such as the bulk pressure – were calculated with no account of position. An early lumped parameter model was proposed by Baer & Frankle, [3].

Piobert's law of burning was recognized at this time which provides a formula for the rate of regression of the solid propellant surface $\dot{r}$ as a function of external gas pressure and a number of empirical constants specific to each propellant type. In addition much effort was devoted towards constructing formulae that would provide the rate of change of burning surface area over time for quite complicated propellant geometries. The idea of the form function was constructed by Corner et al., [2], which provides a relationship between the rate of burning $\dot{r}$ and the exposed surface area S_P . The combination of these two ideas produces a method of measuring the rate of mass-transfer from solid to gas as $\dot{m}=\rho_P S_P \dot{r}$, in which $\dot{m}$ is the rate of gaseous mass addition and ρ_P is the density of the solid propellant. Along with this, an experimentally derived energy of combustion, Q, is taken for the propellant and the rate of energy and pressure increase in the gas-phase can be deduced. During these studies, it was soon apparent that at high pressures the reactant gas could not be described accurately using the ideal gas equation and a co-volume equation was adopted. Both of Piobert's law and Corner's theory are used in internal ballistics modeling today.

However, this approach could not model some of the very noticeable and undesirable phenomena that were being observed during the operation of ballistics weapons, [4]. In particular the presence of longitudinal pressure waves, similar to the combustion instability found in rocket motors, would often cause difficulties and it was crucial to extend the model to at least one-dimension in the axial direction. Kuo & Surnmerfield, [5], first attempted this by developing a one-dimensional inviscid model that included gas dynamics but assumed that the solid propellant remained stationary. Very soon after this, a number of authors, e.g. Krier, [6], Culick, [7], Gough, [8] and Kuo, [9], developed various multiphase flow theories to produce improved models of propellant combustion. However, these were based on different approaches within the multi-phase flow theory. The first two authors adopted the idea that the two-phase mixture acts as a continuum for which equations of mass, momentum and energy can be derived. A thorough documentation of this approach can be found in the book of Soo, [10].

In the late eighties, Gough and associates also extended their work to include kinetics in the XnOVAXKTC gas-phase chemical contained code, [11-12]. The intention was to explain some of the pressure differences obtained when different igniter gases are used to initiate combustion. They were also aware of other phenomena that implied the importance of chemical kinetic such as long ignition delays, often followed by unexplained vigorous combustion, and high reactivity observed in gas-only regions. However, the study does not concentrate on the ignition mechanism but more the effect of different igniter materials on the overall energy release throughout the combustion cycle.

Arguably the most recent breakthrough on propellant combustion was made by Baer & Nunziato, [13], who brought together some of the ideas developed by researchers over previous years. The equations were developed for deflagation-to-detonation transition and had to include compressibility effects in the solid-phase due to the high pressures that occur. The derivation was based on the continuum approach to multi-phase modeling and the resultant system involves mass, momentum and energy equations for both phases and two equations of state. Along with this there is a compaction equation that controls the change in porosity, which was developed to satisfy a number of entropy conditions. From this a well-posed and comprehensive model was developed. For many ballistic scenarios the model of Gough, [8], is sufficient but it is speculated that the equations of Baer & Nunziato, [13], would perform well past the point at which Gough's model fail.

Margolis & Williams have also been investigating the multi-phase flow combustion problem, [14]. In particular they study the effect of a deflagation wave through a propellant bed and include the formation of a liquid-phase. The equations have been mathematically analyzed in the steady-state by use of activation energy asymptotics. However, the development of these ideas for a realistic internal ballistics problem has not so far been pursued.

The wave dynamic phenomena were reviewed by Glass, [15], from the viewpoint of aerodynamics by presenting a series of photographs showing the emergence of a 8 mm diameter bullet from a rifle at a Mach number of 2.0. The interaction between the propellant gas blast and the first blast was described. Detailed visualization of muzzle blasts was reported by Schmidt *et al*., [16], by using a time-resolved, spark shadowgraph technique. The strong coupling between the two blasts was observed, but their interaction was not clearly observable due to the propellant gas being full of dust and smoke. More work, [17], was devoted to modeling of blast wave physics in the region far from the jet flow in terms of well- established theories for spherical blast waves. The work is helpful for sonic boom reduction in military application, but not very useful for understanding wave dynamic processes in the muzzle blasts. Considering that the muzzle blasts are usually characterized by two blast waves, two jet flows, and the shock-wave/moving-body interaction, Jiang *et al*., [18], conducted a numerical study on the muzzle blast by modeling it as a shock-tube-projectile problem. The detailed observation on the wave dynamic processes occurring in the vicinity of the muzzle and around the projectile was reported. From their work, it was found that these wave processes are closely coupled together, and can be neither clearly visualized experimentally because of dusty propellant gases, nor modeled with classic blast theory because of nonlinearity of the wave processes due to complex interactions of various wave phenomena. However, the friction between the projectile and the tube wall was neglected in their work, which results in the second blast being much weaker than in the real physical case.

1.2. Scope of Work

In this investigation we will use a high-fidelity Computational Fluid Dynamics (CFD) model based on Large Eddy Simulations (LES), [19-21], to demonstrate that advanced CFD can be employed to compute gun tube internal ballistics and intermediate ballistics, and that this approach gives added value due to more accurate representation of the flow and shock wave combustion. The use of LES is of course more expensive compared to conventional models, e.g. [11] and compared to Reynolds Averaged Navier Stokes (RANS) models, [22]. A generic gun tube configuration is developed and presented in Section 2. In Section 3 the LES model is described, and in Section 4 the numerical methods are discussed. The numerical methods encompass also the handling of the moving projectile. In Section 5 the computational details of the generic gun tube internal ballistics configuration are presented, and in Section 6 we show some typical results, which are also

used to discuss some of the internal and intermediate ballistics in greater detail. In Section 7 we summarize this work and provide some guidelines for further research.

2 Generic Gun Tube Configuration

The configuration developed here allows us to investigate both the gun tube internal ballistics and the intermediate ballistics. With internal ballistics we here mean motion of a projectile from the time its propellant is ignited until it exits the gun barrel. Similarly, intermediate ballistics is the study of a projectile's behavior from the time it exits the muzzle until the pressure behind the projectile is equalized so it lies between internal ballistics and external ballistics. The objective of this simulation is to study the flow in the gun tube and in the vicinity of the gun tube muzzle. No efforts are made to capture the transition between the intermediate ballistics and the external ballistics.

Figure 2 shows a schematic of the generic gun tube configuration used in the present investigation. The size of the projectile and the gun tube are selected to be in the typical range of a large caliber gun. The projectile has a length of 480 mm and a diameter of 120 mm. The gun tube has a length of 1920 mm (4 projectile lengths), an inner diameter of 134 mm and an outer diameter of 154 mm. It should be noted that the gun tube used here is not rifled but smoothbore, and that the inner diameter is about 10% wider than the projectile. On a real large caliber gun the gun tube is usually fitted with rifles, imposing spin to the projectile around its long axis, in order to gyroscopically stabilize the projectile, improving its aerodynamic stability and accuracy. However, in order to bring down the complexity of the modeling to a manageable level with the existing computational tools the rifling was removed and the gap between the projectile and the barrel was increased.

Figure 2. Schematic of the generic gun-tube configuration including the projectile.

At the start of the simulation, we suppose that the projectile has travelled one projectile length from the breach of the gun tube, and has attained a velocity of 600 m/s, and furthermore we assume that this projectile velocity is constant and maintained throughout the simulation. At the initial time, we do also suppose that all propellant has combusted, and that the volume behind the projectile is filled with high-temperature high-pressure combustion products or propellant gases. More specifically, the combustion products have a temperature of 1800 K, a pressure of 1.8 MPa and a density of 2.0 kg/m^3. Furthermore, the remaining part of the computational domain, including the outer part of the gun tube, is filled with air at standard temperature and pressure, i.e. with a pressure of 100 kPa, a temperature of 298 K and a density of 1.0 kg/m^3. The initial velocity is set to be zero. When the high-temperature high-pressure propellant gases exit the gun tube additional combustion may take place depending on the composition of the propellant gases, sometimes leading to a muzzle flash, but here we assume that the propellant gases are fully combusted during the actual burning of the propellant. This implies that the composition of the propellant gases mainly consists of CO_2 and H_2O.

3 Large Eddy Simulation

The governing equations for interior gun tube ballistics and intermediate ballistics are the balance equations of mass, momentum and energy describing convection, diffusion and reactions, [23]. In LES, these equations are filtered in order to remove the smallest eddy scales, so that the low-pass filtered equations can be resolved on meshs of manageable size. The filtering introduces additional terms in the filtered equations, representing subgrid mass, momentum and energy transfer and modifies the reaction rate terms by averaging these terms over regions of size Δ, where Δ is the filter width. The subgrid terms occur also in non-reacting flows, and may be represented by conventional subgrid flow models, [20, 24], and references therein. The filtered reaction rates are specific to reacting flows, [21, 25-28], in which mixing and chemical reactions are closely related, typically occurring on scales smaller than Δ, necessitating modeling of these processes taking into account the effects of the subgrid turbulence chemistry interactions.

The reactive LES equations are derived by low-pass filtering the reactive mass, momentum and energy equations, and after re-arranging the terms these equations are,

$$\begin{cases} \partial_t(\bar{\rho})+\nabla\cdot(\bar{\rho}\tilde{\mathbf{v}})=0, \\ \partial_t(\bar{\rho}\tilde{Y}_i)+\nabla\cdot(\bar{\rho}\tilde{\mathbf{v}}\tilde{Y}_i)=\nabla\cdot(\bar{\mathbf{j}}_i-\mathbf{b}_i)+\overline{\dot{w}_i}, \\ \partial_t(\bar{\rho}\tilde{\mathbf{v}})+\nabla\cdot(\bar{\rho}\tilde{\mathbf{v}}\otimes\tilde{\mathbf{v}})=-\nabla\bar{p}+\nabla\cdot(\bar{\mathbf{S}}-\mathbf{B}), \\ \partial_t(\bar{\rho}\tilde{E})+\nabla\cdot(\bar{\rho}\tilde{\mathbf{v}}\tilde{E})=\nabla\cdot(-\bar{p}\tilde{\mathbf{v}}+\tilde{\mathbf{S}}\tilde{\mathbf{v}}+\bar{\mathbf{h}}-\mathbf{b}_E)+\bar{\rho}\tilde{\sigma}, \end{cases} \tag{1}$$

in which $\bar{\rho}$, $\tilde{Y}_i$, $\tilde{\mathbf{v}}$ and $\tilde{E}$ are the filtered density, species mass fractions, velocity and total energy, respectively. Here, following conventional practice, overbars denote filtering and tildes denote Favre filtering, [19]. The gas mixture is assumed to be ideal, linearly viscous, with Fourier heat conduction and Fickian diffusion so that $\bar{p}=\bar{\rho}R\tilde{T}$, $\bar{\mathbf{S}}=2\mu\tilde{\mathbf{D}}_D$, $\bar{\mathbf{h}}=\kappa\nabla\tilde{T}$ and $\bar{\mathbf{j}}_i=D_i\nabla\tilde{Y}_i$, in which R is the composition dependent gas constant, $\tilde{\mathbf{D}}_D$ the deviatoric part of the rate-of-strain tensor $\tilde{\mathbf{D}}$. The viscosity, μ, is modeled by Sutherland's law, and the species' and thermal diffusivities are modeled as $D_i=\mu/Sc_i$ and $\kappa=\mu/Pr$, respectively, in which Sc_i and Pr are the Schmidt and Prandtl numbers. The subgrid stress tensor and flux vectors (responsible for the unresolved transport) are defined by $\mathbf{B}=\bar{\rho}(\widetilde{\mathbf{v}\otimes\mathbf{v}}-\tilde{\mathbf{v}}\otimes\tilde{\mathbf{v}})$, $\mathbf{b}_i=\bar{\rho}(\widetilde{\mathbf{v}Y_i}-\tilde{\mathbf{v}}\tilde{Y}_i)$ and $\mathbf{b}_E=\bar{\rho}(\widetilde{\mathbf{v}E}-\tilde{\mathbf{v}}\tilde{E})$, respectively. The filtered temperature, $\tilde{T}$, results from solving the filtered equation-of-state for the total energy, $\tilde{E}=\tilde{h}-\bar{p}/\bar{\rho}+\frac{1}{2}\tilde{\mathbf{v}}^2+k$, in which $k=\frac{1}{2}(\widetilde{\mathbf{v}^2}-\tilde{\mathbf{v}}^2)$ is the subgrid kinetic energy and $\tilde{h}=\Sigma_i(\tilde{Y}_i h_{i,f}^{\theta})+\Sigma_i(\tilde{Y}_i\int_{T_0}^{\tilde{T}}C_{p,i}(T)dT)$ the enthalpy, with $h_{i,f}^{\theta}$ the enthalpies of formation and $C_{p,i}$ the (temperature dependent) specific heats. The filtered species reaction rates are defined by $\overline{\dot{w}_i}=M_iP_{ij}\overline{\dot{w}_j}$, in which M_i is the molar mass of specie i, P_{ij} the stoichiometric coefficients and $\dot{w}_j$ the reaction rate of reaction j.

The subgrid stress tensor and flux vectors $\mathbf{B}$, $\mathbf{b}_i$ and $\mathbf{b}_E$ can be modeled by most models discussed in [24], and references therein, that also provide estimates of the subgrid kinetic energy, k, which often is required in the modeling of the turbulence chemistry interactions or the filtered reaction rates $\overline{\dot{w}_i}$. Based on comparison with experimental data, the preferred model is the linear combination or Mixed Model (MM), [29-30], in which,

$$\mathbf{B}=\bar{\rho}(\tilde{\mathbf{v}}\widetilde{\otimes}\tilde{\mathbf{v}}-\tilde{\tilde{\mathbf{v}}}\otimes\tilde{\tilde{\mathbf{v}}})-2\mu_k\tilde{\mathbf{D}}_D,\quad \mathbf{b}_i=\bar{\rho}(\widetilde{\tilde{\mathbf{v}}\tilde{Y}_i}-\tilde{\tilde{\mathbf{v}}}\tilde{\tilde{Y}}_i)-\frac{\mu_k}{Sc_t}\nabla\tilde{Y}_i,\quad \mathbf{b}_E=\bar{\rho}(\widetilde{\tilde{\mathbf{v}}\tilde{E}}-\tilde{\tilde{\mathbf{v}}}\tilde{\tilde{E}})-\frac{\mu_k}{Pr_t}\nabla\tilde{E}, \tag{2}$$

in which the subgrid viscosity, $\mu_k=c_k\bar{\rho}\Delta k^{1/2}$, is obtained from solving the modeled k-equation which takes the following form,

$$\partial_t(\bar{\rho}k)+\nabla\cdot(\bar{\rho}k\tilde{\mathbf{v}})=2c_k\bar{\rho}\Delta k^{1/2}\|\tilde{\mathbf{D}}\|^2+\nabla\cdot(\mu_k\nabla k)-\bar{\rho}c_\varepsilon k^{3/2}/\Delta, \tag{3}$$

in which Sc_t and Pr_t are the turbulent Schmidt and Prandtl numbers. The model coefficients, c_k and c_ε, are derived from an inertial range spectra, $E(\kappa)=C_\kappa\varepsilon^{2/3}\kappa^{-5/3}$, so that $c_k=0.07$ and $c_\varepsilon=1.05$, respectively. To reduce the computational cost *wall-modeled* LES is recommended, in which a subgrid wall model is used to handle the near-wall flow physics, [31]. The model employed here is based on modifying the filter width, Δ, in the modeled k-equation (3) and in the equation for the subgrid viscosity according to the expression $\Delta=\min(\kappa y_w f(u_\tau,y_w),\ V_P^{1/3})$, with κ being the von-Karman constant, y_w the distance to the wall, u_τ the friction velocity estimated from Spalding's law, $f(u_\tau,y_w)$ a non-linear damping function and V_P the volume of the control volume P, to take into account the quenching of eddy motions by the presence of the wall. Although a very simple but robust model it has proven reliable and accurate, and is found to scale correctly with decreasing values of y_w.

The modeling of the filtered reaction rates used here is based on the Partially Stirred Reactor (PaSR) model, [32], in which the flow is divided into fine structures (*) and surroundings (^{0}), with characteristic dimensions of the fine structures being small compared to the mesh spacing, Δ. Since molecular mixing occurs at the fine structures, most reactions also take place here. On an LES level, the intrinsic topology of the fine structures is insignificant, provided that it is possible to accurately estimate the fine-structure (or reacting) volume fraction γ^*, so that the filtered reaction rate of reaction step j can be conveniently expressed as,

$$\begin{aligned}\overline{\dot{w}_j(\rho,T,Y_i)}&=\int_\rho\int_T\int_{Y_i}\wp(\rho,T,Y_i)\dot{w}_j(\rho,T,Y_i)d\rho dT dY_i=\\ &\gamma^*\dot{w}_j(\bar{\rho},T^*,Y_i^*)+(1-\gamma^*)\dot{w}_j(\bar{\rho},T^0,Y_i^0),\end{aligned} \tag{4}$$

in which $\wp(\rho,T,Y_i)$ is a N+2 dimensional probability density function. The conditions in the fine structures and surroundings are related through the subgrid (mass and energy) balance equations $\bar{\rho}(Y_i^*-Y_i^0)/\tau^*\approx\dot{w}_i(\bar{\rho},Y_i^*,T^*)$ and $\bar{\rho}\Sigma_{i=1}^N(Y_i^*h_i^*-Y_i^0h_i^0)/\tau^*=\Sigma_{i=1}^N h_{i,f}^\theta\dot{w}_i(\bar{\rho},Y_i^*,T^*)$, respectively, in which τ^* is the fine structure residence time. By defining the resolved fields ($\tilde{}$) as $\tilde{Y}_i=\gamma^*Y_i^*+(1-\gamma^*)Y_i^0$ and $\tilde{T}=\gamma^*T^*+(1-\gamma^*)T^0$, the subgrid (mass and energy) balance equations become,

$$\begin{cases}\bar{\rho}(Y_i^*-\tilde{Y}_i)=(1-\gamma^*)\tau^*\dot{w}_i(\bar{\rho},Y_i^*,T^*),\\ \bar{\rho}\Sigma_{i=1}^N(Y_i^*h_i^*(T^*)-\tilde{Y}_i\tilde{h}_i(\tilde{T}))=(1-\gamma^*)\tau^*\Sigma_{i=1}^N h_{i,f}^\theta\dot{w}_i(\bar{\rho},Y_i^*,T^*).\end{cases} \tag{5}$$

The fine-structure reacting volume fraction is defined as $\gamma^*=\Delta V^*/\Delta^3$, in which Δ^3 is the cell volume, in which the LES variables are constant. This implies that we may lump the fine structure and surrounding fluid components together in different parts of the LES cell. The lumped fine structures are collectively described by the chemical time scale, τ_c, as the reactions are assumed to take place within these structures. Since the dependent variables are constant in each LES cell, the fine structure volume can be approximated as $\Delta V^*=\Delta^2|\tilde{\mathbf{v}}|\tau_c$. Similarly, the cell volume can be estimated as $\Delta^3=\Delta^2|\tilde{\mathbf{v}}|(\tau_c+\tau^*)$, in which τ^* is the fine structure residence time. The definition of the fine-structure reacting volume fraction then results in,

$$\gamma^*=\tau_c/(\tau_c+\tau^*). \tag{6}$$

In (6) the chemical time scale should be representative of the overall combustion reaction, and is here represented by $\tau_c\approx\delta_u/s_u\approx\nu/s_u^2$, in which δ_u and s_u are the laminar flame thickness

and speed. The modeling of the fine-structure residence time, τ^*, is based on the observations that the fine-structure area to volume ratio, $\Delta S^*/\Delta V^*$, is defined by the dissipative length scale $\ell_D=(\nu\Delta/v')^{1/2}$, determined by the molecular viscosity, ν, and the subgrid velocity stretch v'/Δ, and that the velocity influencing these structures is the Kolmogorov velocity, v_K, such that $\tau^*=\ell_D/v_K$. Combining the expressions for ℓ_D and v_K, utilizing the Kolmogorov length and time scales, $\ell_K=(\nu^3/\varepsilon)^{1/4}$, and $\tau_K=(\nu/\varepsilon)^{1/2}$, in which $\varepsilon=(v')^3/\Delta$ is the dissipation, finally results in that,

$$\tau^*=\sqrt{\tau_\Delta\tau_K}=\nu^{1/4}\Delta^{3/4}v'^{-5/4}, \tag{7}$$

in which $\tau_\Delta=\Delta/v'$. This time scale was recently found by Yeung *et al*, [33], to accurately model the statistics of dissipation, and therefore also of small-scale mixing.

4 Numerical Methods

For this study we use the C++ library OpenFoam, [34], as the computational platform, which has previously been used for applications of varying complexity, e.g. [20, 21, 28, 30-32, 35-39]. The code employs an unstructured collocated Finite Volume (FV) method, [34], in which the discretization is based on Gauss theorem together with a fully explicit time-integration scheme. Given the vector of unknowns, $\bar{\mathbf{u}}=[\bar{\rho}, \bar{\rho}\tilde{Y}_i, \bar{\rho}\tilde{\mathbf{v}}, \bar{\rho}\tilde{E}]^T$, the discretized equations can be compactly summarized as,

$$\begin{cases} \bar{\mathbf{u}}^* = \bar{\mathbf{u}}^n - \Delta t\left(\frac{1}{\delta V_P}\Sigma_f[\mathbf{F}_f^C(\bar{\mathbf{u}}^n) - \mathbf{F}_f^D(\bar{\mathbf{u}}^n) + \mathbf{F}_f^B(\bar{\mathbf{u}}^n)] - \mathbf{s}_P(\bar{\mathbf{u}}^n)\right), \\ \bar{\mathbf{u}}^{n+1} = \frac{1}{2}(\bar{\mathbf{u}}^n + \bar{\mathbf{u}}^*) - \frac{1}{2}\Delta t\left(\frac{1}{\delta V_P}\Sigma_f[\mathbf{F}_f^C(\bar{\mathbf{u}}^*) - \mathbf{F}_f^D(\bar{\mathbf{u}}^*) + \mathbf{F}_f^B(\bar{\mathbf{u}}^*)] - \mathbf{s}_P(\bar{\mathbf{u}}^*)\right), \end{cases} \tag{8}$$

where $\mathbf{F}_f^C(\bar{\mathbf{u}})=[\bar{\rho}\tilde{\mathbf{v}}, \bar{\rho}\tilde{\mathbf{v}}\otimes\mathbf{v}, \bar{\rho}\tilde{\mathbf{v}}E, \bar{\rho}\tilde{\mathbf{v}}Y_i]^T\cdot d\mathbf{A}_f$, $\mathbf{F}_f^D(\bar{\mathbf{u}})=[0, \bar{p}\mathbf{I}-\bar{\mathbf{S}}, \bar{\rho}\tilde{\mathbf{v}}\tilde{E}+\bar{p}\tilde{\mathbf{v}}-\bar{\mathbf{S}}\tilde{\mathbf{v}}-\bar{\mathbf{h}}, -\bar{\mathbf{j}}_i]^T\cdot d\mathbf{A}_f$, $\mathbf{F}_f^B(\bar{\mathbf{u}})=[0, \mathbf{B}, \mathbf{b}, \mathbf{b}_i]^T\cdot d\mathbf{A}_f$ and $s_P(\bar{\mathbf{u}})=[0, \mathbf{0}, 0, \bar{\dot{w}}_i]^T$ are the convective, diffusive, subgrid fluxes and source terms, respectively. For the convective fluxes, $\mathbf{F}_f^C(\bar{\mathbf{u}})$, a monotonicity preserving reconstruction of the form $\mathbf{F}_f^C(\bar{\mathbf{u}})=\mathbf{F}_f^{C,H}(\bar{\mathbf{u}})-(1-\Psi(\bar{\mathbf{u}}))[\mathbf{F}_f^{C,H}(\bar{\mathbf{u}})-\mathbf{F}_f^{C,L}(\bar{\mathbf{u}})]$ is used, [40], in which $\mathbf{F}_f^{C,H}(\bar{\mathbf{u}})$ denotes a 2nd order linear reconstruction, $\mathbf{F}_f^{C,L}(\bar{\mathbf{u}})$ a 1st order upwind biased reconstruction and $\Psi=\Psi(\bar{\mathbf{u}})$ a non-linear flux limiter. The non-linear flux limiter is used to switch between the two underlying reconstruction algorithms, and here the MC limiter, [40], is used for the momentum, energy and species equations whereas only the higher order scheme is used for the continuity equation. To minimize the non-orthogonality errors in the viscous and subgrid fluxes, $\mathbf{F}_f^D(\bar{\mathbf{u}})$ and $\mathbf{F}_f^B(\mathbf{u},\bar{\mathbf{u}})$, respectively, these are split into orthogonal and non-orthogonal parts, [40]. Central difference approximation and gradient face interpolation are used for the orthogonal and non-orthogonal parts respectively. The equations are solved sequentially, with iteration over the non-linear source terms to obtain rapid convergence.

In order to model the motion of the projectile inside the gun tube, during the exit, and outside the gun tube, we use a method of deforming grids, coupled with remeshing and interpolation. This is a variation of a methodology that has previously been developed at FOI for simulating rotating propellers appended to ship hulls, [41]. In this method we allow the computational grid be deformed as the moving boundaries move, as illustrated in Figure 3.

Before the mesh is so deformed that it introduces numerical errors, we stop the simulation, and regenerate the mesh with the moving parts, in this case the projectile, in its new position. Then we interpolate the solution from the old grid to the new grid, and the simulation is restarted. This method can be broken down in the following steps for the present case:

1. Determine the position of the projectile at the instants when the mesh needs to be changed. To do this, we simulate the moving projectile using a single mesh, while monitoring the mesh quality and the behaviour of the solver (the number of iterations and the residuals). From this we determine for how long interval the mesh can be used before the mesh quality affects the solution. We then apply a safety margin to this interval.
2. Set up the initial conditions and boundary conditions on the mesh for the domain at the initial time.
3. Advance the solution in time, solving the discretized equations and deforming the mesh.
4. When the projectile has reached the position for the next mesh change, interrupt the time-stepping.

5. Switch mesh and interpolate the solution to the new mesh. Continue from step 3.

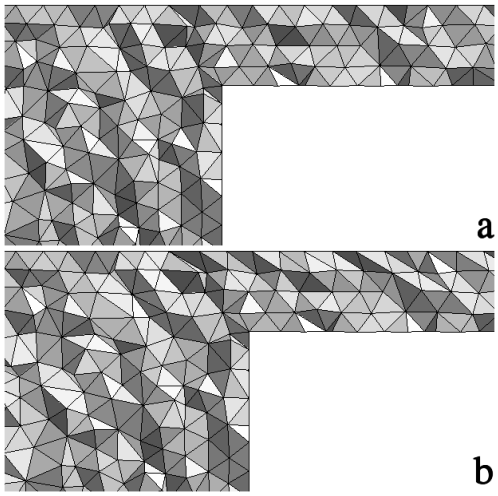

Figure 3. A cut through the computational mesh, showing a part of the back of the projectile. In (a) the solution has been mapped to a new mesh, and in (b) the same mesh has been deformed, especially above the projectile, and the projectile has moved to the right.

The grid motion is performed using a "Laplacian mesh motion method" implemented in OpenFOAM. At the boundaries of the domain, the mesh motion is prescribed. For this case, the grid motion velocity at the projectile boundary is the projectile velocity, and the grid motion velocity at all other boundaries is zero. At the interior of the domain, the mesh motion is required to fulfill an elliptic equation, $\nabla\cdot(\gamma\nabla\mathbf{v}_{grid})=0$, where $\mathbf{v}_{grid}$ is the grid motion velocity, and γ is a grid motion diffusivity coefficient which can be constant or variable. For this simulation case the grid motion diffusivity coefficient is the inverse quadratic distance to the projectile. The account for the moving mesh, some modifications are made to the discretized equations. The integral form of the conservarvation equation for a variable, ψ, can be written as,

$$\partial_t \int_\Omega \bar{\rho}\tilde{\psi}dV+\int_{\partial\Omega}\bar{\rho}\tilde{\psi}(\tilde{\mathbf{v}}-\mathbf{v}_{mesh})\cdot dA=\int_\Omega S_\psi dV, \tag{9}$$

in which S_ψ denotes the sources and sinks of the variable ψ. Discretizing (9) results in that,

$$(\bar{\rho}_P\tilde{\psi}_P\tilde{\mathbf{v}}_P)^{n+1}-(\bar{\rho}_P\tilde{\psi}_P\tilde{\mathbf{v}}_P)^{n}+\Delta t\Sigma_f\rho_f(\mathbf{F}-\mathbf{F}_{grid})\psi_f, \tag{10}$$

in which the superscripts n and n+1 denote the present and next time steps, respectively, and in which the subscript f denote evaluation at cell face f, and P denote evaluation at cell center P. Moreover, $\mathbf{F}$ is the convective fluid flux and $\mathbf{F}_{grid}$ is the grid motion flux. The difference to the conservation equation on a static computational grid is that the cell volume in the time derivative is not constant and the mesh motion flux is introduced in the equation. These variables must fulfill the so-called space conservation law, stating that

$$\partial_t \int_\Omega dV-\int_{\partial\Omega}\mathbf{v}_{mesh}\cdot dA=0. \tag{11}$$

In order to ensure that that this is fulfilled in the discretized form,

$$V_P^{n+1}-V_P^n-\Delta t\Sigma_f\mathbf{F}_{grid}, \tag{12}$$

we compute the grid motion flux $\mathbf{F}_{grid}$ as the volume swept by the moving face, divided by

the time step length. For simulation involving mesh motion in OpenFOAM, the convective fluxes are updated to $\mathbf{F}-\mathbf{F}_{\text{grid}}$. The mesh motion implementation in OpenFOAM is described in further detail in [42].

5 Computational Set-Up

The computational domain is a cylindrical sector of 45 degrees shown schematically in figure 4. The computational domain has a length of 4.8 m and a radius of 2.4 m. The part of the domain outside of the gun tube starts at half the length of the gun tube, two projectile lengths from the gun tube muzzle. As described in section 2, the projectile has a length of 480 mm and a diameter of 120 mm. The gun tube has a length of 1920 mm (4 projectile lengths), an inner diameter of 134 mm and an outer diameter of 154 mm.

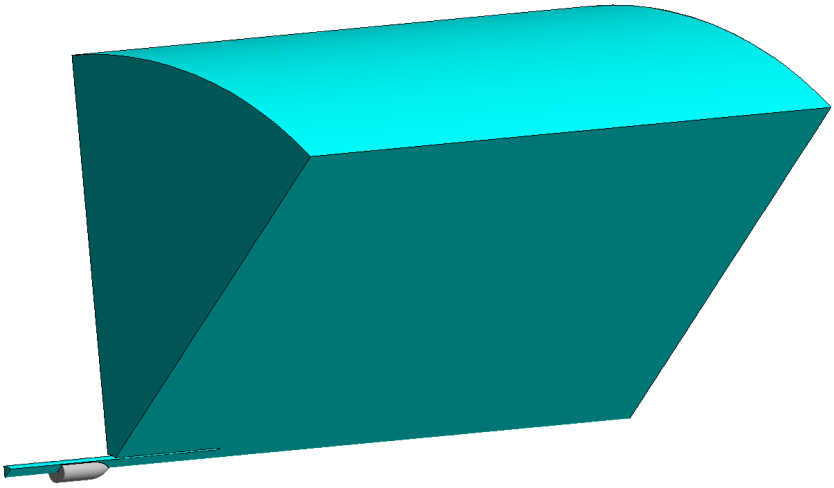

Figure 4. The computational domain employed.

The reason to introduce a small gap between the projectile and the gun tube is to overcome issues regarding generating a computational mesh on this domain. In a real case we do not have such a large gap, but as illustrated in figure 5, the small angle between the projectile and the gun tube, and the small distance between the projectile and gun tube makes it very difficult to generate a working computational grid for such a domain. More specifically, as seen in figure 5a, the angle between the wall of the gun tube and the projectile is very small at the point where the tapering of the projectile starts which prevents sufficiently good grid quality in this part of the domain. Moreover, at the time when the end of the gun tube meets the projectile boundary, see figure 5b, and when the end of the projectile is just separated from the gun tube, see figure 5c, the cell size required would be the distance travelled by the projectile in one time step, which is not feasible.

The computational grid is a tetrahedral grid of variable mesh density, with a low resolution in the parts of the domain where the shockwave generated by the moving projectile has not yet reached. At the start of the simulation the computational grid has 0.8 million cells, and at the instant the projectile exits from the gun tube, the computational grid has 33.0 million cells. When the projectile is inside the gun tube, we must interpolate the solution to a new computational mesh every 2.4 mm. The meshes are generated automatically. After the projectile has exited from the gun tube, the intervals between required remeshing are longer. When the projectile has moved 1/10 of a projectile length from the opening of the gun tube the interval between mesh changes can be doubled. Figure 6 shows the computational mesh at four instants of the simulation.

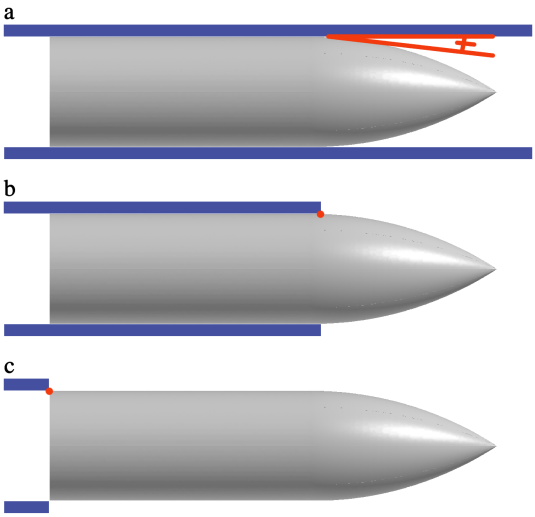

Figure 5. Illustration of practical problems when generating the computational mesh for simulation of a projectile exiting a gun tube.

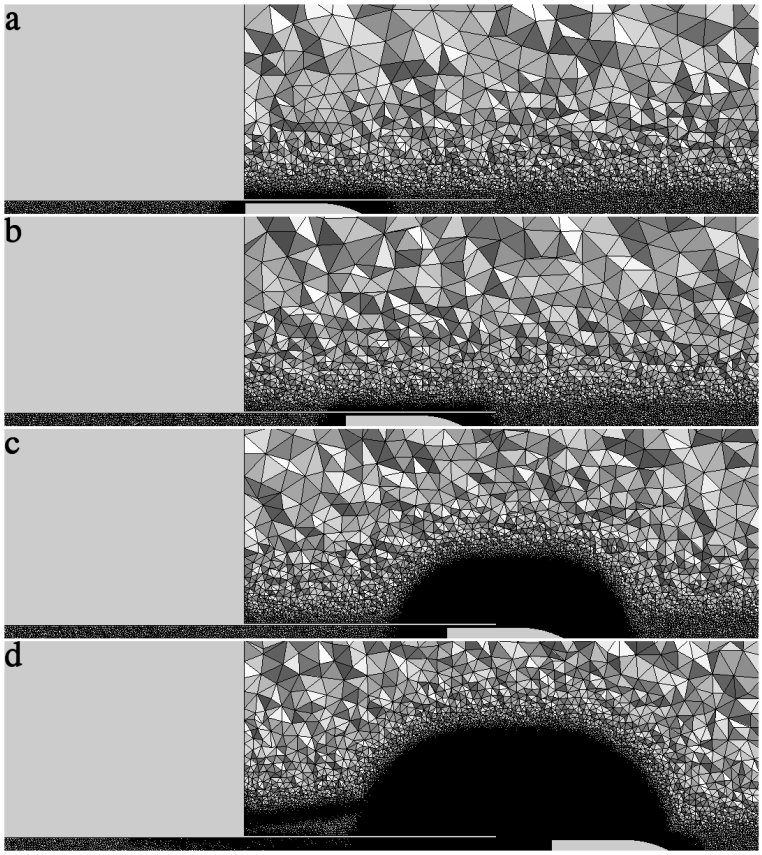

Figure 6. The computational mesh at (a) t=0.0008 s, 2 projectile lengths from the gun tube breach (b) t=0.0014 s, 2.8 projectile lengths from the gun tube breach, (c) t=0.0021 s, 3.6 projectile lengths from the gun tube breach, and (d) t=0.0027 s, 4.4 projectile lengths from the gun tube breach.

The initial fields are set up as described in section 2 in the interior of the domain. In Figure 7 the corresponding boundary patches used are illustrated. At the side patches of the cylindrical sector, FRONT and BACK, we use periodic boundary conditions for all variables. At the outflow patch, OUTFLOW, Dirichlet conditions for the pressure, temperature and

density are employed. For the patches GUNTUBE, PROJECTILE and FARFIELD, zero Neumann conditions for the pressure, temperature and density are employed. For the velocity, Dirichlet conditions are applied at the PROJECTILE patch, whereas at all other patches zero Neumann conditions are applied.

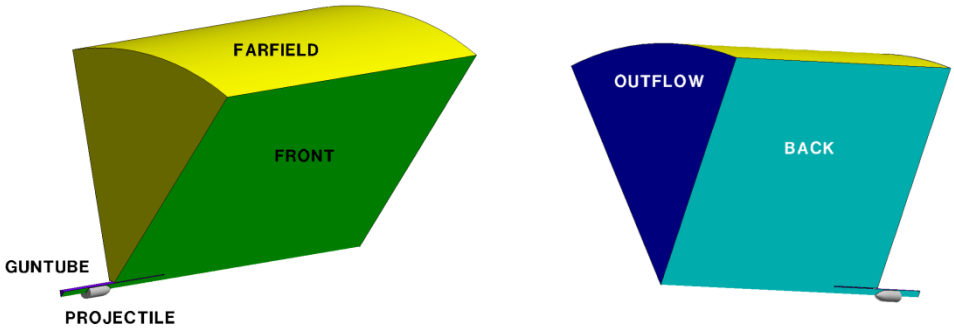

Figure 7. The boundary patches. The whole projectile is shown in this figure, even if the projectile boundary patch only is a 45 degrees sector.

6 Results

The wave dynamic processes occurring in the gun tube, during which the projectiles travels through the gun tube, and in the muzzle blast flow are schematically shown in figure 1. A precursor shock wave driven by the projectile propagates through the gun tube and ahead of the projectile that acts like a piston. The pressure is higher behind the projectile and lower in front of it due to the friction force between the projectile and the shock tube wall, which maintains a balance between the driving and the drag forces acting on the projectile. When the precursor shock wave discharges from the open end, the first blast develops, which results in shock-wave diffraction with an associated initiation of a vortex ring and a jet flow. Later, the projectile itself moves out and away from the gun tube and interacts with the diffracting shock system and the jet flow. Meanwhile, the high-pressure high-temperature propellant gas behind the projectile expands out of the shock tube and the second blast develops. The second blast can overtake the projectile and the first blast, but these two blasts will eventually be overtaken by the projectile. So, this flow is characterized by two blast waves, two jet flows, and a bow shock.

Since this computational study is primarily focusing on demonstrating the computational methodology the simulations are not pursued long enough for all these physical features to be present in the computational results. The simulations are terminated some time after the projectile has exited the gun tube, pushing the precursor shock ahead of it, and with the secondary blast being developed between the muzzle and the rear of the projectile.

The time evolution of the computational grid is presented in figure 6. As described previously the computational grid continuously deforms and is regenerated every 2.4 mm but is also adapted to capture the evolving shock wave system. This implies that the grid resolution is significantly finer across and behind the bow shock, resulting in high resolution of the jet and secondary flow features developing after the projectile has exited the gun tube.

To visualize the evolving flow and the progressing shock-wave systems we use the magnitude of the pressure gradient, $|\nabla p|$. Figure 8 shows a time sequence of $|\nabla p|$ at (a) t=8 ms, (b) t=14 ms, (c) t=21 ms and (d) t=27 ms after the projectile has left its original position. These times corresponds to 2, 2.8, 3.6 and 4.4 projectile lengths from the gun tube breach. Figures 8a and 8b shows the evolution of the projectile in the gun tube, pushing the precursor shock wave in front of itself, and revealing a shock wave pattern developing along the nose section of the projectile. High-pressure gradients are also observed in the gap between the gun tube wall and the projectile. These pressure gradients would not occur in a real gun due to the much smaller clearance between the gun tube wall and the projectile, and the presence of the rifling. Behind the projectile the pressure is decreasing as the volume between the projectile and the breach is increasing. In figure 8c the projectile is seen exiting the gun tube. Prior to the projectile exiting the gun tube the precursor shock has exited the gun tube. The high-pressure high temperature gas behind the projectile expands out of the gun tube in the gap between the projectile and the gun tube walls whereas the precursor shock wave expands radially in all directions. The precursor shock is almost spherically symmetric as it expands, but is stronger just in front of the muzzle as it is pushed forward by the projectile. The second blast can be seen forming halfway along the projectile, at the end of the gun tube. A contact discontinuity can also be observed following the transition from the nose of the projectile to the cylindrical midsection. In figure 8d the projectile has completely exited the gun tube. The high-pressure gas behind the projectile now expands out of the gun tube across its whole cross section, whereas the precursor shock wave continues to expand radially in all directions. The second blast wave is now under rapid development, and consists of a leading shock wave, a contact surface, and an

expansion fan. The wave system propagates outward, mainly in a radial direction but also parallel to the projectile. Meanwhile, the projectile moves inside the first jet where the particle velocity is almost equal to the projectile speed, therefore, there is nothing observable in front of the projectile. The precursor shock wave, the contact surface, and the secondary upward-facing shock in the first blast are approximately spherical in shape. The bow shock is located very close to the projectile because of its shape, and if the projectile nose would have been more blunt the distance between the nose of the projectile and the blow shock would have been significantly larger.

A rather strong toroidal vortex system is observed to develop just outside of the gun muzzle due to the high-pressure high temperature propellant gas exiting the gun tube behind the projectile. This vortex system creates significant large-scale mixing between the high temperature propellant gas and the surrounding air, and if the conditions are appropriate afterburning may take place at the gun muzzle. This flash is highly undesirable and can be eliminated by using muzzle breaks.

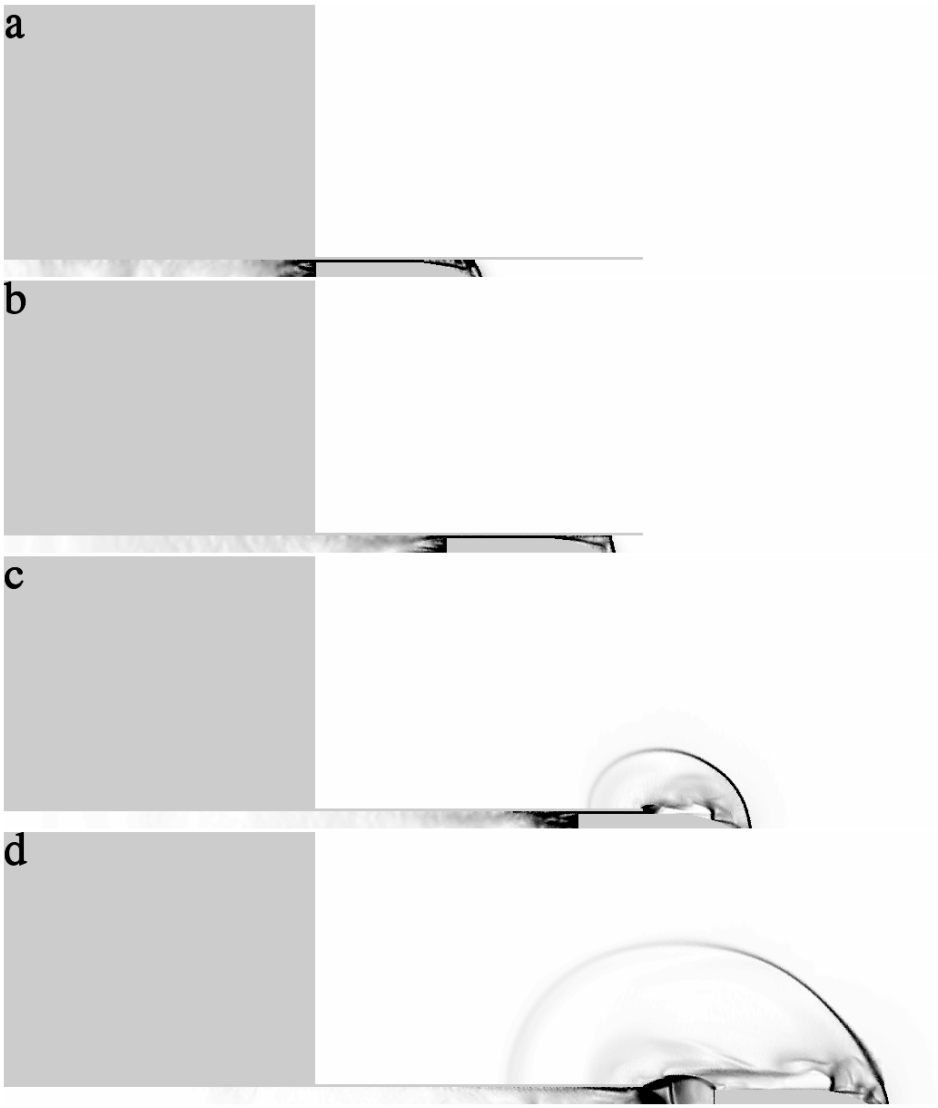

Figure 8. Magnitude of the pressure gradient at (a) t=0.0008 s, 2 projectile lengths from the gun tube breach (b) t=0.0014 s, 2.8 projectile lengths from the gun tube breach, (c) t=0.0021 s, 3.6 projectile lengths from the gun tube breach, and (d) t=0.0027 s, 4.4 projectile lengths from the gun tube breach.

7 Concluding Remarks

In this work we have presented a numerical simulation technique for unsteady gun tube flows based on a Large Eddy Simulation (LES) model coupled with a deformation and regeneration technique for handling the motion of the projectile through the gun tube and into the external domain in which the gun tube is embedded. A generic, and rather simple, gun tube configuration, without rifling and muzzle break, has been used to demonstrate this technique. The computational domain consists of a cylindrical sector of 45 degrees and extends about ten projectile lengths outside of the gun muzzle. The deformation and regeneration technique used for handling the motion of the projectile have been developed for handling rotating propellers behind ships but is general enough to also deal with translational motions of arbitrary rigid objects. The computational overhead using this approach is about 10%. In addition to using the deformation and regeneration technique, semi-adaptive grid refinement is also used to improve the spatial resolution between the precursor bow shock and the gun tube.

From the simulation results some analysis is presented regarding the flow within the gun tube and just outside the muzzle. A precursor shock wave driven by the projectile propagates through the gun tube and ahead of the projectile that acts like a piston. The pressure is higher behind the projectile and lower in front of it due to the friction force between the projectile and the shock tube wall, which maintains a balance between the driving and the drag forces acting on the projectile. When the precursor shock wave discharges from the open end, the first blast develops, which results in shock-wave diffraction with an associated initiation of a vortex ring and a jet flow. Later, the projectile itself moves out and away from the gun tube and interacts with the diffracting shock system and the jet flow. Meanwhile, the high-pressure high-temperature propellant gas behind the projectile expands out of the shock tube and the second blast develops.

The simulation results presented here should be extended further in time in order to examine the flow physics of gun launch in greater detail.

The deformation and regeneration technique used for handling the motion of the projectile should be compared against sliding mesh or overset grid techniques recently available in OpenFoam. The sliding grid technique may be more advantageous since it can more accurately handle the very narrow gap between the gun tube walls and the projectile.

References

[1] Krier H. & Summerfield M.; 1979, "Interior Ballistics of Guns", Progress in Astronautics and Aeronautics Series, 66.

[2] Corber, G.B.; 1951, "Internal Ballistics", Ministry of Supply Scientific Advisory Council, H.M. Stationnary Office.

[31 Baer P.G. & Frankle J.M.; 1963, "The Simulation of Interior Ballistic Performance of Guns by Digital Computer Program", Technical Report BRL-1183, Ballistics Research Laboratory, Aberdeen Proving Ground, MD.

[4] May X.Y. & Horst X,Y.; 1979, "Gun Design and Pressure Waves", Progress in Astronautics and Aeronautics Series, 66, p 177.

[5] Kuo K.K. & Surnmerfield M.; 1974, "Theory of Steady-State Burning of Gas-permeable Propellants", AIAA, 12, p 49.

[6] Krier H.; 1976, "Predictions of Pressure Wave Propagation and Flame Fronts in Reactive Solid-Gas Mixtures", Proc. Two-phase Transport and Reactor Safety, Fort Lauerdale, October, HemispherePub. Corp.

[7] Culick F.E.C.; 1975, "Conservation Equations for a Reacting Two-Phase Flow based on Continuum Theory. Proc. 12th JANNAF Combustion Meeting.

[8] Gough P.S.; 1974, "The Flow of a Compressible Gas through an Aggregate of Mobile Reacting Particles", McGill University, Dept. Mechanical Engineering.

[9] Kuo K.K, Koo J.H., Davis T.R. & Coates G.R.; 1976, "Transient Combustion in Mobile Gas-permeable Propellants", Acta Astronautica, **3**, p 573.

[10] Soo S.L.; 1967, "Fluid Dynamics of Multiphase Systems". Waltham.

[11] Horst A.W. & Keller G.E.; 1987, "A Two-phase Flow Simulation of LOVA Propellant Interior Ballistic Behavior using the XnOVAK Code", Technical Report BRL-TR-2796, Ballistics Research Laboratory, Aberdeen Proving Ground, MD.

[12] Keller G.E., Horst A.W. & Gough P.S.; 1990, "New Directions in Multiphase Flow Interior Ballistic Modeling", Technical Report BRL-TR-3102, Ballistics Research Laboratory, Aberdeen Proving Ground, MD.

[13] Baer M.R. & Nunziato J.W.; 1986, "A Two-Phase Mixture Theory for the Deflagation-to-Detonation Transition (DDT) in Reactive Granular Materials", J. Multiphase Flow, **12**, p 861.

[14] Margolis S. & Williams F.A.; 1990, "Effects of Two-Phase Flow in a Model for Nitramine Deflagation", Comb. Flame, **80**, p 329.

[15] Glass I.I.; 1974, "Shock Waves and Man", The University of Toronto Press, Toronto.

[16] Schmidt E. & Shear D.; 1975, "Optical Measurements of Muzzle Blast", AIAA J. **13**, p 1086.

[17] Merlen A. & Dyment A.; 1991, "Similarity and Asymptotic Analysis for Gun-Firing Aerodynamics", J. Fluid Mech. **225**, p 497.

[18] Jiang Z., Takayama K. & Skews B.W.;, "Numerical Study on Blast Flowfields Induced by Supersonic Projectiles Discharged from Shock Tubes", Phys. Fluids **10**, p 277.

[19] Sagaut P.; 2001, "Large Eddy Simulation for Incompressible Flows", Springer Verlag, Heidelberg, FRG.

[20] Grinstein F.F., Margolin L. & Rider B. (Eds.); 2007, "Implicit Large Eddy Simulation: Computing Turbulent Fluid Dynamics", Cambridge University Press, New York, USA.

[21] Menon S. & Fureby C.; 2010, "Computational Combustion", In Encyclopedia of Aerospace Engineering, Eds. Blockley R. & Shyy W., John Wiley & Sons.

[22] Wilcox D.C.; 2000, "Turbulence Modeling for CFD", 2nd Ed., DCW Industries Inc.

[23] Oran E.S. & Boris J.P.; 1987, "Numerical Simulation of Reactive Flow", Elsevier, New York.

[24] Sagaut P.; 2001, "Large Eddy Simulation for Incompressible Flows", Springer Verlag, Heidelberg, FRG.

[25] Bray K.N.C.; 1996, "The Challenge of Turbulent Combustion", 26th Int. Symp. on Comb., The Combustion Institute, Pittsburgh, USA, p 1.

[26] Echekki T.; 2009, “Multiscale Methods in Turbulent Combustion: Strategies and Computational Challenges”, Comp. Sci. & Discovery, **2**, p .
[27] Oefelein J.C., Drozda T.G. & Sankaran V.; 2006, “Large Eddy Simulation of Turbulence-Chemistry Interactions in Reacting Flows”, J. Phys. Conf. Ser., 48, p 16.
[28] Fureby C.; 2009, “LES Modeling of Combustion for Propulsion Applications”, Phil.. Trans. R. Soc. A, **367**, p 2957.
[29] Bardina J., Ferziger J.H. & Reynolds W.C.; 1980, “Improved Subgrid Scale Models for Large Eddy Simulations”, AIAA Paper 80-1357.
[30] Bensow R. & Fureby C.; 2007, “On the Justification and Extension of Mixed Models in LES”, J. Turb. **8**, p 54.
[31] Fureby C.; 2007, “On LES and DES of Wall Bounded Flows”, Ercoftac Bulletin, March issue.
[32] Sabelnikov V. & Fureby C.; 2013, “LES Combustion Modeling for High Re Flames using a Multi-Phase Analogy”, Comb. Flame, **160**, p 83.
[33] Yeung P.K., Pope S.B. & Sawford B.L.; 2006, “Reynolds Number Dependence of Lagrangian Statistics in Large Numerical Simulations of Isotropic turbulence”, J. Turb., **7**, p 1.
[34] Weller H.G., Tabor G., Jasak H. & Fureby C.; 1997, “A Tensorial Approach to CFD using Object Oriented Techniques“, Comp. in Physics, **12**, p 629.
[35] Fureby C.; 2009, “LES Modeling of Combustion for Propulsion Applications”, Presented at the Applied Large Eddy Simulation Workshop at the Royal Society, London, UK. Phil. Trans. R. Soc. A, **367**, p 2957.
[36] Berglund M. & Fureby C.; 2005, “LES of Supersonic Combustion in a Scramjet Engine Model”, 31st Int. Symp on Comb., p 2491.
[37] Fureby C., Chapuis M., Fedina E. Karl S.; 2011, “CFD Analysis of the Hyshot II Combustor” Proc. Comb. Inst., **33**, p 2399.
[38] Fedina E., Fureby C., Borzov S.A., Gusev V.N., Stepanova T.V.; 2011, “Combustion LES of CESAR Multi-Burner Annular Combustor”, AIAA 2011-0785.
[39] Fedina E. & Fureby C.; 2011, “A Compartive Study of Flamelet and Finite Rate Chemistry LES of an Axisymmetrc Dump Combustor”, J. Turb, **12**, N54.
[40] Drikakis D., Fureby C., Grinstein F.F. & Liefendahl M.; 2007, “ILES with Limiting Algorithms”, In Implicit Large Eddy Simulation: Computing Turbulent Fluid Dynamics, Eds. Grinstein F.F., Margolin L. & Rider B., Cambridge University Press, p 94.
[41] Liefvendahl M. Troëng C.; 2007, “Deformation and Regeneration of the Computational Grid for CFD with Moving Boundaries”, AIAA-2007-1458.
[42] Jasak H. & Tukovic Z.; 2007, “Automatic Mesh Motion for the Unstructured Finite Volume Method”, Transactions of FAMENA, **30**, N2

FOI, Swedish Defence Research Agency, is a mainly assignment-funded agency under the Ministry of Defence. The core activities are research, method and technology development, as well as studies conducted in the interests of Swedish defence and the safety and security of society. The organisation employs approximately 1000 personnel of whom about 800 are scientists. This makes FOI Sweden's largest research institute. FOI gives its customers access to leading-edge expertise in a large number of fields such as security policy studies, defence and security related analyses, the assessment of various types of threat, systems for control and management of crises, protection against and management of hazardous substances, IT security and the potential offered by new sensors.

FOI
Defence Research Agency
SE-164 90 Stockholm

Phone: +46 8 555 030 00
Fax: +46 8 555 031 00

www.foi.se